Coherent diffractive photoproduction of ρ^0 mesons on gold nuclei at RHIC

L. Adamczyk[1], J. K. Adkins[20], G. Agakishiev[18], M. M. Aggarwal[33], Z. Ahammed[50], I. Alekseev[16,28], D. M. Anderson[44], R. Aoyama[3], A. Aparin[18], D. Arkhipkin[3], E. C. Aschenauer[3], M. U. Ashraf[47], A. Attri[33], G. S. Averichev[18], X. Bai[7], V. Bairathi[29], R. Bellwied[46], A. Bhasin[17], A. K. Bhati[33], P. Bhattarai[45], J. Bielcik[10], J. Bielcikova[11], L. C. Bland[3], I. G. Bordyuzhin[16], J. Bouchet[19], J. D. Brandenburg[38], A. V. Brandin[28], I. Bunzarov[18], J. Butterworth[38], H. Caines[54], M. Calderón de la Barca Sánchez[5], J. M. Campbell[31], D. Cebra[5], I. Chakaberia[3], P. Chaloupka[10], Z. Chang[44], A. Chatterjee[50], S. Chattopadhyay[50], J. H. Chen[41], X. Chen[23], J. Cheng[47], M. Cherney[9], W. Christie[3], G. Contin[24], H. J. Crawford[4], S. Das[13], L. C. De Silva[9], R. R. Debbe[3], T. G. Dedovich[18], J. Deng[40], A. A. Derevschikov[35], B. di Ruzza[3], L. Didenko[3], C. Dilks[34], X. Dong[24], J. L. Drachenberg[22], J. E. Draper[5], C. M. Du[23], L. E. Dunkelberger[6], J. C. Dunlop[3], L. G. Efimov[18], J. Engelage[4], G. Eppley[38], R. Esha[6], S. Esumi[3], O. Evdokimov[8], O. Eyser[3], R. Fatemi[20], S. Fazio[3], P. Federic[11], J. Fedorisin[18], Z. Feng[7], P. Filip[18], Y. Fisyak[3], C. E. Flores[5], L. Fulek[1], C. A. Gagliardi[44], D. Garand[36], F. Geurts[38], A. Gibson[49], M. Girard[51], L. Greiner[24], D. Grosnick[49], D. S. Gunarathne[43], Y. Guo[39], A. Gupta[17], S. Gupta[17], W. Guryn[3], A. I. Hamad[19], A. Hamed[44], R. Haque[29], J. W. Harris[54], L. He[36], S. Heppelmann[5], S. Heppelmann[34], A. Hirsch[36], G. W. Hoffmann[45], S. Horvat[54], H. Z. Huang[6], T. Huang[30], B. Huang[8], X. Huang[47], P. Huck[7], T. J. Humanic[31], G. Igo[6], W. W. Jacobs[15], H. Jang[21], A. Jentsch[45], J. Jia[3,42], K. Jiang[39], E. G. Judd[4], S. Kabana[19], D. Kalinkin[15], K. Kang[47], K. Kauder[52], H. W. Ke[3], D. Keane[19], A. Kechechyan[18], Z. H. Khan[8], D. P. Kikoła [51], I. Kisel[12], A. Kisiel[51], L. Kochenda[28], D. D. Koetke[49], L. K. Kosarzewski[51], A. F. Kraishan[43], P. Kravtsov[28], K. Krueger[2], L. Kumar[33], M. A. C. Lamont[3], J. M. Landgraf[3], K. D. Landry[6], J. Lauret[3], A. Lebedev[3], R. Lednicky[18], J. H. Lee[3], X. Li[43], C. Li[39], Y. Li[47], W. Li[41], X. Li[39], T. Lin[15], M. A. Lisa[31], Y. Liu[44], F. Liu[7], T. Ljubicic[3], W. J. Llope[52], M. Lomnitz[19], R. S. Longacre[3], X. Luo[7], S. Luo[8], R. Ma[3], L. Ma[41], G. L. Ma[41], Y. G. Ma[41], N. Magdy[42], R. Majka[54], A. Manion[24], S. Margetis[19], C. Markert[45], H. S. Matis[24], D. McDonald[46], S. McKinzie[24], K. Meehan[5], J. C. Mei[40], Z. W. Miller[8], N. G. Minaev[35], S. Mioduszewski[44], D. Mishra[29], B. Mohanty[29], M. M. Mondal[44], D. A. Morozov[35], M. K. Mustafa[24], B. K. Nandi[14], Md. Nasim[6], T. K. Nayak[50], G. Nigmatkulov[28], T. Niida[52], L. V. Nogach[35], S. Y. Noh[21], T. Nonaka[3], J. Novak[27], S. B. Nurushev[35], G. Odyniec[24], A. Ogawa[3], K. Oh[37], V. A. Okorokov[28], D. Olvitt Jr.[43], B. S. Page[3], R. Pak[3], Y. X. Pan[6], Y. Pandit[8], Y. Panebratsev[18], B. Pawlik[32], H. Pei[7], C. Perkins[4], P. Pile[3], J. Pluta[51], K. Poniatowska[51], J. Porter[24], M. Posik[43], A. M. Poskanzer[24], N. K. Pruthi[33], M. Przybycien[1], J. Putschke[52], H. Qiu[36],

Preprint submitted to Elsevier *October 21, 2016*

A. Quintero[43], S. Ramachandran[20], R. L. Ray[45], R. Reed[25,25], H. G. Ritter[24], J. B. Roberts[38], O. V. Rogachevskiy[18], J. L. Romero[5], L. Ruan[3], J. Rusnak[11], O. Rusnakova[10], N. R. Sahoo[44], P. K. Sahu[13], I. Sakrejda[24], S. Salur[24], J. Sandweiss[54], A. Sarkar[14], J. Schambach[45], R. P. Scharenberg[36], A. M. Schmah[24], W. B. Schmidke[3], N. Schmitz[26], J. Seger[9], P. Seyboth[26], N. Shah[41], E. Shahaliev[18], P. V. Shanmuganathan[19], M. Shao[39], A. Sharma[17], B. Sharma[33], M. K. Sharma[17], W. Q. Shen[41], S. S. Shi[7], Z. Shi[24], Q. Y. Shou[41], E. P. Sichtermann[24], R. Sikora[1], M. Simko[11], S. Singha[19], M. J. Skoby[15], N. Smirnov[54], D. Smirnov[3], W. Solyst[15], L. Song[46], P. Sorensen[3], H. M. Spinka[2], B. Srivastava[36], T. D. S. Stanislaus[49], M. Stepanov[36], R. Stock[12], M. Strikhanov[28], B. Stringfellow[36], T. Sugiura[3], M. Sumbera[11], B. Summa[34], Z. Sun[23], Y. Sun[39], X. M. Sun[7], B. Surrow[43], D. N. Svirida[16], Z. Tang[39], A. H. Tang[3], T. Tarnowsky[27], A. Tawfik[53], J. Thäder[24], J. H. Thomas[24], A. R. Timmins[46], D. Tlusty[38], T. Todoroki[3], M. Tokarev[18], S. Trentalange[6], R. E. Tribble[44], P. Tribedy[3], S. K. Tripathy[13], O. D. Tsai[6], T. Ullrich[3], D. G. Underwood[2], I. Upsal[31], G. Van Buren[3], G. van Nieuwenhuizen[3], M. Vandenbroucke[43], R. Varma[14], A. N. Vasiliev[35], R. Vertesi[11], F. Videbæk[3], S. Vokal[18], S. A. Voloshin[52], A. Vossen[15], G. Wang[6], F. Wang[36], J. S. Wang[23], Y. Wang[7], H. Wang[3], Y. Wang[47], J. C. Webb[3], G. Webb[3], L. Wen[6], G. D. Westfall[27], H. Wieman[24], S. W. Wissink[15], R. Witt[48], Y. Wu[19], Z. G. Xiao[47], G. Xie[39], W. Xie[36], K. Xin[38], Z. Xu[3], Y. F. Xu[41], Q. H. Xu[40], N. Xu[24], J. Xu[7], H. Xu[23], Q. Yang[39], Y. Yang[23], Y. Yang[7], C. Yang[39], Y. Yang[30], S. Yang[39], Z. Ye[8], Z. Ye[8], L. Yi[54], K. Yip[3], I. -K. Yoo[37], N. Yu[7], H. Zbroszczyk[51], W. Zha[39], Z. Zhang[41], X. P. Zhang[47], Y. Zhang[39], J. B. Zhang[7], J. Zhang[40], S. Zhang[41], J. Zhang[23], S. Zhang[39], J. Zhao[36], C. Zhong[41], L. Zhou[39], X. Zhu[47], Y. Zoulkarneeva[18], M. Zyzak[12]

[1] *AGH University of Science and Technology, FPACS, Cracow 30-059, Poland*

[2] *Argonne National Laboratory, Argonne, Illinois 60439*

[3] *Brookhaven National Laboratory, Upton, New York 11973*

[4] *University of California, Berkeley, California 94720*

[5] *University of California, Davis, California 95616*

[6] *University of California, Los Angeles, California 90095*

[7] *Central China Normal University, Wuhan, Hubei 430079*

[8] *University of Illinois at Chicago, Chicago, Illinois 60607*

[9] *Creighton University, Omaha, Nebraska 68178*

[10] *Czech Technical University in Prague, FNSPE, Prague, 115 19, Czech Republic*

[11] *Nuclear Physics Institute AS CR, 250 68 Prague, Czech Republic*

[12] *Frankfurt Institute for Advanced Studies FIAS, Frankfurt 60438, Germany*

[13] *Institute of Physics, Bhubaneswar 751005, India*

[14] *Indian Institute of Technology, Mumbai 400076, India*

[15]*Indiana University, Bloomington, Indiana 47408*
[16]*Alikhanov Institute for Theoretical and Experimental Physics, Moscow 117218, Russia*
[17]*University of Jammu, Jammu 180001, India*
[18]*Joint Institute for Nuclear Research, Dubna, 141 980, Russia*
[19]*Kent State University, Kent, Ohio 44242*
[20]*University of Kentucky, Lexington, Kentucky, 40506-0055*
[21]*Korea Institute of Science and Technology Information, Daejeon 305-701, Korea*
[22]*Lamar University, Physics Department, Beaumont, Texas 77710*
[23]*Institute of Modern Physics, Chinese Academy of Sciences, Lanzhou, Gansu 730000*
[24]*Lawrence Berkeley National Laboratory, Berkeley, California 94720*
[25]*Lehigh University, Bethlehem, PA, 18015*
[26]*Max-Planck-Institut fur Physik, Munich 80805, Germany*
[27]*Michigan State University, East Lansing, Michigan 48824*
[28]*National Research Nuclear University MEPhI, Moscow 115409, Russia*
[29]*National Institute of Science Education and Research, Bhubaneswar 751005, India*
[30]*National Cheng Kung University, Tainan 70101*
[31]*Ohio State University, Columbus, Ohio 43210*
[32]*Institute of Nuclear Physics PAN, Cracow 31-342, Poland*
[33]*Panjab University, Chandigarh 160014, India*
[34]*Pennsylvania State University, University Park, Pennsylvania 16802*
[35]*Institute of High Energy Physics, Protvino 142281, Russia*
[36]*Purdue University, West Lafayette, Indiana 47907*
[37]*Pusan National University, Pusan 46241, Korea*
[38]*Rice University, Houston, Texas 77251*
[39]*University of Science and Technology of China, Hefei, Anhui 230026*
[40]*Shandong University, Jinan, Shandong 250100*
[41]*Shanghai Institute of Applied Physics, Chinese Academy of Sciences, Shanghai 201800*
[42]*State University Of New York, Stony Brook, NY 11794*
[43]*Temple University, Philadelphia, Pennsylvania 19122*
[44]*Texas A&M University, College Station, Texas 77843*
[45]*University of Texas, Austin, Texas 78712*
[46]*University of Houston, Houston, Texas 77204*
[47]*Tsinghua University, Beijing 100084*
[48]*United States Naval Academy, Annapolis, Maryland, 21402*
[49]*Valparaiso University, Valparaiso, Indiana 46383*

[50] *Variable Energy Cyclotron Centre, Kolkata 700064, India*
[51] *Warsaw University of Technology, Warsaw 00-661, Poland*
[52] *Wayne State University, Detroit, Michigan 48201*
[53] *World Laboratory for Cosmology and Particle Physics (WLCAPP), Cairo 11571, Egypt*
[54] *Yale University, New Haven, Connecticut 06520*

Abstract

The STAR Collaboration reports on the photoproduction of $\pi^+\pi^-$ pairs in gold-gold collisions at a center of mass energy of 200 GeV/nucleon. These pairs are produced when a nearly-real photon emitted by one ion scatters from the other ion. We fit the $\pi^+\pi^-$ mass spectrum to a combination of ρ^0 and ω resonances and a direct $\pi^+\pi^-$ continuum; the ratio of ρ^0 to direct $\pi^+\pi^-$ is consistent with previous measurements. The ω cross section is comparable with that expected from the measured $\gamma p \to \omega p$ cross section, a classical Glauber calculation and the $\omega \to \pi^+\pi^-$ branching ratio. The ρ^0 differential cross section $d\sigma/dt$ clearly exhibits a diffraction pattern, compatible with scattering from a gold nucleus, with 2 minima visible.

Keywords: rho photo-production, omega photoproduction, direct pion pair photoproduction, diffraction, hadronic form factor
PACS: 25.75.Dw, 25.20.Lj, 13.60.-r

1. Introduction

Relativistic heavy ions are accompanied by high photon fluxes due to their large electric charge and the strongly Lorentz contracted electric fields. These photons are nearly real, with virtuality $\langle Q^2 \rangle \sim 2 \times 10^{-3}\text{GeV}^2$.

In relativistic heavy ion collisions, these fields can produce photonuclear interactions. When the nuclei collide and interact hadronically, the strong interactions obscure these electromagnetic interactions. However, when they physically miss each other, the photonuclear interactions can be seen; these are refered to as Ultra-Peripheral Collisions (UPCs). The photon flux is well described within the Weizsäcker-Williams formalism [1, 2].

For photoproduction of ρ mesons at RHIC, the rapidity range $|y| < 0.7$ corresponds to photon-nucleon center of mass energies from 9 to 18 GeV, depending on the rapidity and final state transverse momentum. In this region, the ρ^0 photo-production cross section increases slowly with collision energy and the $\gamma p \to \rho p$ cross section is well described by the soft-Pomeron model [3].

A more detailed model of vector meson photoproduction considers the photon as a combination of Fock states: a bare photon with virtual $q\overline{q}$ pairs, plus higher virtual states. It was successful at describing many of the Deep Inelastic Scattering (DIS) measurements performed at HERA [4] and is also applicable in the UPC environment.

Many models have been proposed to describe the ρ photoproduction cross section in ultra-peripheral heavy ion collisions. The first calculation used HERA data on $\gamma p \to \rho p$ as input to a classical Glauber calculation to predict the cross section with heavy ions [5]. It successfully predicted the ρ photoproduction cross section at RHIC energies from 62 GeV/nucleon [6] to 130 [7] and 200 GeV/nucleon [8], and up to 2.76 TeV/nucleon at the LHC [9]. A later calculation treated the $q\bar{q}$ pair as a dipole in a quantum Glauber calculation, which found a cross section about 50% higher, in tension with the data [10]. Recently, a modification of the quantum Glauber calculation has been proposed; in this model nuclear shadowing reduces the calculated ρ cross section to match the data [11]. Other calculations include nuclear saturation mechanisms, including the colored glass condensate [12, 13]. Two-photon production of $\pi^+\pi^-$ pairs also occurs, but the cross section is much smaller than for photonuclear interactions [14].

Because of the high photon flux these UPC events have a high probability to be accompanied by additional photon exchanges that excite one or both of the ions, into Giant Dipole Resonances (GDR) or higher excitations. The GDRs typically decay by emitting a single neutron, while higher resonances usually decay by emitting two or more neutrons [15]. These neutrons have low momentum with respect to their parent ion, so largely retain the beam rapidity. For heavy nuclei, the cross section for multi-photon interactions nearly factorizes [16] , with the combined cross section given by an integral over impact parameter space:

$$\sigma(A_1A_2 \to A_1^*A_2^*\rho) = \int d^2b P_{0\mathrm{Had}}(b) P_1(b, A^*) P_2(b, A^*) P(b, \rho), \tag{1}$$

where $P_{0\mathrm{Had}}(b)$, $P_1(b, A^*)$, $P_2 b, (A^*)$ and $P(b, \rho)$ are the respective probabilities for not having a hadronic interaction, exciting each of the ions and producing a ρ. Each photon-mediated reaction occurs via independent photon exchange, so all four probabilities are tied together only through a common impact parameter [17]. The photonuclear cross sections are based on parameterized data [18]. The individual photon-mediated subreactions have a strong impact parameter dependence, so the combined probability is highest for impact parameters $b >\approx 2R_A$, where R_A is the nuclear radius. A unitarization process is employed to account for the possibility of multiple photons contributing to excite a single nucleus.

This letter reports on the measurement of exclusive ρ and ω meson and direct $\pi^+\pi^-$ photo-production in UPCs between gold ions using the Solenoidal Tracker At RHIC (STAR) detector at a center of mass energy of 200 GeV/nucleon. The current data sample is about 100 times larger than in previous measurements [8] at this energy. The improved statistics allow for much higher precision studies, leading to two main new results. First, the high-statistics $\pi\pi$ invariant mass distribution cannot be fit with just ρ and direct $\pi\pi$ components; an additional contribution from photoproduction of ω, with $\omega \rightarrow \pi^+\pi^-$ is required for an acceptable fit. The second is the observation of a detailed diffraction pattern, clearly showing the first and second minima, with a possible third. This diffraction pattern can be used to determine the distribution of the hadronic matter in gold nuclei.

2. Experimental Setup and Analysis

This analysis uses an integrated luminosity of $1074 \pm 107 \mu b^{-1}$ of data collected during 2010. Five STAR components were used for triggering and event reconstruction in the analysis: the Time Projection Chamber (TPC), Time of Flight system (TOF), Beam Beam Counters (BBCs) and East and West Zero Degree Calorimeters (ZDCs).

The STAR TPC [19] efficiently detects charged tracks with pseudo-rapidities $|\eta| < 1.4$, using 45 layers of pad rows in a 2 m long cylinder. In the 0.5 T solenoidal magnetic field, the momentum resolution is $\Delta p/p = 0.005 + 0.004p$ with p in GeV/c [19]. The TPC can also identify charged particles by their specific ionization energy loss (dE/dx) in the TPC. The dE/dx resolution is 8% for a track that crosses 40 pad rows. This gives good pion/kaon/proton separation up to their respective rest masses. The TPC is surrounded by a time of flight system (TOF), covering pseudo-rapidity up to $|\eta| < 1$ [20]. For this analysis, the TOF system was used to reject tracks that are out of time with the beam crossing.

The other detector components were used solely for triggering. At higher rapidities, charged particles are detected using the two BBCs, one on each side of the nominal interaction point. Each is formed with 18 scintillator tiles arranged around the beam pipe, covering a pseudo-rapidity window of $2 < |\eta| < 5$ [21]. The ZDCs are small hadron calorimeters installed downstream of the collision region to detect neutrons at beam rapidity [22].

The trigger [23] selected 38 million events with small multiplicity in the central detector, along with one or more neutrons in each ZDC, along the lines described in [8]. It requires low activity in the TOF detector (at least two and no more than six hits), no charged particles detected in the BBC detectors and finally, showers in both ZDC detectors corresponding to at least the equivalent of one neutron with beam momentum or up to four beam momentum neutrons. The threshold on each ZDC calorimeter was set at 50 ADC channels (the centroid of the one neutron peak sits at 198 channels) making them fully efficient.

The analysis selected events containing a pair of oppositely charged tracks that were consistent with originating from a single vertex, located within 50 cm longitudinally of the center of the interaction region. The tracks were required to have at least 14 hits in the TPC (out of a possible 45), and have dE/dx values within 3σ of the expected dE/dx for a pion. Both tracks in each pair were required to have a valid hit in the TOF system; this cut rejected events from other beam crossings. It also limited the track acceptance largely to the region $|\eta| < 1.0$. The 384,000 events with a $\pi^+\pi^-$ pair mass in the range $0.25 < M_{\pi\pi} < 1.5$ GeV were saved for further evalutation.

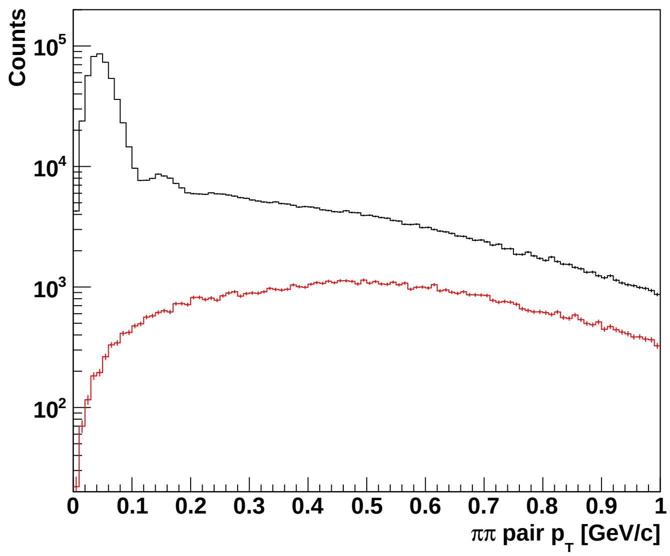

Figure 1: The black histogram shows the pion pair transverse momentum. The peak below 100 MeV/c is from coherently produced $\pi^+\pi^-$ pairs. The red histogram shows the pair momentum for same-sign pion pairs. Both histograms show pairs that come from vertices with only two tracks.

The largest backgrounds for this analysis were low-multiplicity hadronic interactions (peripheral ion-ion collisions), with some of their charged particles out of the TPC acceptance. Other backgrounds come from other UPC reactions or from cosmic-rays accompanied by in-time mutual Coulomb exitation. Pure electromagnetic production of e^+e^- pairs contribute less than 4% to the ρ peak [7]. The decay $\omega \to \pi^+\pi^-\pi^0$ produces a $\pi^+\pi^-$ pair with a larger p_T than for coherent photoproduciton, and a pair invariant mass that is usually below 600 MeV. It was a 2.7% background in a previous analysis [8], and should be smaller here. We neglect these minor backgrounds here; they are well within the overall systematic errors.

The hadronic backgrounds may be estimated from the like-sign pion pairs. Figure 1 compares the transverse momentum (p_T) of the $\pi^+\pi^-$ pairs (black histogram) with the corresponding distribution for like-sign pairs (red histogram) in recorded vertices with only two tracks. The signal distribution has a prominent peak for $p_T < 100$ MeV/c. This peak is due to coherent photoproduction of pion pairs from the gold nucleus. In this region, the signal to noise ratio is very high; at larger p_T, the backgrounds are a larger fraction of the signal.

The reconstructed events are corrected for acceptance and detection efficiency using a detailed simulation of the STAR detector. A mix of ρ mesons and non-resonant $\pi\pi$ events are generated using the STARLight Monte Carlo [24, 5] which reproduces the kinematics of the event, including the mass and rapidity distributions. These events are sent through a complete GEANT simulation of the detector and then embedded in 'zero bias' STAR events. Zero-bias events are data from randomly selected beam crossings. This embedding procedure accurately accounts for the detector noise and backgrounds, including overlapping events recorded in the STAR TPC during its sizeable active time windows. As Fig. 2 shows, the agreement between the Monte Carlo and data is very good.

The efficiency depends only weakly on the pair mass and pair p_T, but depends fairly strongly on rapidity. The rapidity dependence has a bell shape with a maximum of 13% efficiency at $y \approx 0.1$. It is slightly asymmetric because of inefficiencies on one of the TPC West (rapidity < 0) sectors. A major uncertainty in the reconstruction efficiency stems from uncertainties in the actual ('as-built') positions of the TOF slats, which may not be completely accurately reflected in the simulations. While this uncertainty may affect the measured $d\sigma/dy$, particularly at large rapidity, it does not significantly affect the pair p_T or mass acceptance uncertainties.

The two ZDC calorimeters detect the neutrons emitted by both beams in mutual electromagnetic dissociation with efficiency close to 100% and energy resolution sufficient to separate up to three neutron peaks. Figure 3 shows the ADC distribution from the West ZDC for events that satisfy a cut which selects events with a single neutron in the East ZDC and a photoproduced ρ^0 with $|y| < 1$ and $p_T < 100$ MeV/c.

This analysis considers two classes of nuclear breakup: single neutrons (1n), associated with Giant Dipole Resonances, or any number of neutrons (Xn), from a broad range of photonuclear interactions. The trigger selected events with one to four neutrons in each ZDC. This led to a relatively high yield of photoproduced ρ^0 per trigger, but did not cover the full neutron number spectrum. So, we used the 1n1n events to normalize the XnXn cross section, based on the STARlight calculation of the cross section ratio. We find the ratio of triggered events to those with single neutrons in each ZDC, using the fit results in Table 1, and use the STARlight ratio of XnXn to 1n1n events to normalize the overall cross section scale.

The cross sections in Table 1 decrease slowly with increasing total neutron number. The summed cross section for $2\mathrm{n}1\mathrm{n} + 1\mathrm{n}2\mathrm{n}$ (*i.e.* the two combinations with 1 neutron in one direction, is 83% of the 1n1n cross section. This fraction is larger than is seen for mutual Coulomb dissociation, where one calculation has the $2\mathrm{n}1\mathrm{n} + 1\mathrm{n}2\mathrm{n}$: 1n1n ratio around 0.6 [25] and another finds a ratio around 0.4, albeit at a slightly lower beam energy [26]. Some of this difference is because the requirement of ρ photoproduction selects events with smaller impact parameters, where the photon spectrum is harder [16].

3. The $\pi^+\pi^-$ Mass Spectrum and $d\sigma/dt$

Figure 4 shows the efficiency-corrected, like-sign-pair (background) subtracted invariant-mass of the pion pairs with $p_T < 100$ MeV/c. Events with dipion mass $M_{\pi\pi} > 600$ MeV/c^2 were initially fitted with a modified Söding parametrization

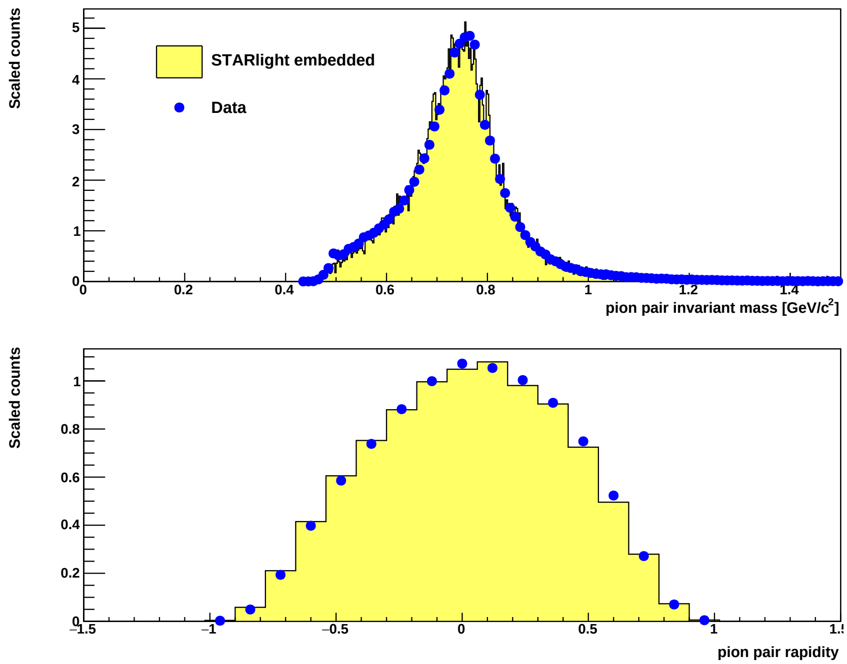

Figure 2: Comparison of uncorrected data (blue points) with embedded simulated ρ^0 and direct $\pi\pi$ events (yellow histogram). The simulated UPCs were run through a GEANT simulation of the detector, embedded in randomly triggered (zero-bias) events, and subject to the same reconstruction programs as the data.

[27] which included a relativistic Breit-Wigner resonance for the ρ^0 plus a flat direct $\pi^+\pi^-$ continuum. This 2-component model was a poor fit to the data ($\chi^2/DOF = 633/298$), so an additional relativistic Breit-Wigner component was added, to account for ω photoproduction, followed by its decay $\omega \rightarrow \pi^+\pi^-$. This leads to the following fit function:

$$\frac{d\sigma}{dM_{\pi^+\pi^-}} \propto \left| A_\rho \frac{\sqrt{M_{\pi\pi} M_\rho \Gamma_\rho}}{M_{\pi\pi}^2 - M_\rho^2 + iM_\rho\Gamma_\rho} + B_{\pi\pi} + C_\omega e^{i\phi_\omega} \frac{\sqrt{M_{\pi\pi} M_\omega \Gamma_{\omega\rightarrow\pi\pi}}}{M_{\pi\pi}^2 - M_\omega^2 + iM_\omega\Gamma_\omega} \right|^2 + f_p \tag{2}$$

where A_ρ is the ρ amplitude, $B_{\pi\pi}$ is the amplitude for the direct pions and C_ω is the amplitude for the ω. The momentum-dependent widths in Eqs. (3) and (4) below are motivated by the forms proposed in Alvensleben *et al.* [28], where Γ_0 is the pole width for each meson. Several variations of the di-pion mass dependence for the ω width were tried, but none were significantly different from a constant, reflecting the fact that the ω width is small, and the width does not change significantly in that mass range. The momentum-dependent

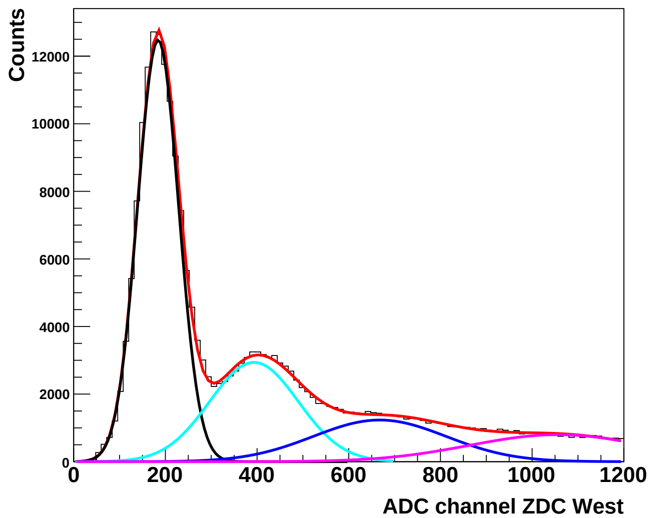

Figure 3: The shower energy in the West ZDC by neutron produced by mutual dissociation is shown as a distribution of ADC channels. These events had a single neutron detected on the East ZDC. The peaks corresponding to 1 to 4 neutrons are fitted with Gaussian distributions with standard deviations that grow as $n\sigma$ with n the number of neutrons and σ the standard deviation of the one neutron Gaussian. The red curve is the sum of all Gaussians which are also displayed individually.

widths are taken to be

$$\Gamma_\rho = \Gamma_0 \frac{M_\rho}{M_{\pi\pi}} \left(\frac{M_{\pi\pi}^2 - 4m_\pi^2}{M_\rho^2 - 4m_\pi^2} \right)^{3/2} \tag{3}$$

and

$$\Gamma_\omega = \Gamma_0 \frac{M_\omega}{M_{\pi\pi}} \left(\frac{M_{\pi\pi}^2 - 9m_\pi^2}{M_\omega^2 - 9m_\pi^2} \right)^{n}, \tag{4}$$

where Γ_0 is the pole width for each meson. For the ω, the $9m_\pi^2$ term reflects the fact that the ω decay is dominated by the three-pion channel, $n = 3/2$ for a quasi-two-body decay and $n = 4$ for a free-space three-body decay [29, 30]. We have tested Γ as constant, and the $n = 3/2$ and $n = 4$ cases. All three fits result in negligible difference due to the narrow width of ω decay, and we choose a default Γ with $n = 3/2$ for all the fits shown in the figures and extracted values. The branching ratio for $\omega \to \pi^+\pi^-$ is small, so we use

$$\Gamma_{\omega\to\pi\pi} = \mathrm{Br}(\omega \to \pi\pi)\Gamma_0 \frac{M_\omega}{M_{\pi\pi}} \left(\frac{M_{\pi\pi}^2 - 4m_\pi^2}{M_\omega^2 - 4m_\pi^2} \right)^{3/2} \tag{5}$$

with $\mathrm{Br}(\omega \to \pi\pi) = 0.0153^{+0.11}_{-0.13}$ [31].

East ZDC	West ZDC		
	1n	2n	3n
1n	1.38 ± 0.24 mb	0.57 ± 0.11 mb	0.39 ± 0.07 mb
2n	0.57 ± 0.11 mb	0.23 ± 0.04 mb	0.18 ± 0.03 mb
3n	0.40 ± 0.07 mb	0.19 ± 0.03 mb	0.15 ± 0.03 mb

Table 1: Mutual dissociation cross sections for events with exclusive coherent ρ^0 photoproduction. The row number shows the number of neutrons detected in the East ZDC and the column number lists the number of neutrons detected in the West ZDC. The cross sections are determined by applying an appropriate window to one ZDC spectrum and measuring the neutron spectrum in the other, and then reversing the procedure. The two results are averaged, and the difference gives the systematic error. Statistical errors are small ($< 1\%$) and are not listed. Systematic errors arising from the cuts used to select the events were added in quadrature to the sum in quadrature of the relevant common uncertainties listed in Tab. 4 (17%).

In Eq. 2 f_p is a linear function that describes the remaining remnant background. The masses and widths of the ρ and ω were allowed to float, making for a total of ten parameters: four masses/widths, three amplitudes, the phase of the ω meson, and two parameters for the polynomial background.

In Fig. 4, the fitted ρ component is shown by the full blue line, with the direct $\pi\pi$ component shown in dashed black, while the interference between the two components is shown by the dashed blue lines. The full red line shows the fitted ω component and the dashed red line shows the interference between the ρ^0 and the ω components.

Table 2 shows the fit results. The ρ and ω masses and the ρ width are in good agreement with their generally accepted values [31]. The ω is considerably wider than the standard value, because it is broadened by the detector resolution. At the ω peak, the detector resolution is about 8.5 MeV/c^2, comparable to the ρ width. The fit $\chi^2/DOF = 255/270$ shows that the data and model are consistent in the fit region of 0.6 to 1.3 GeV/c^2.

The ratio of ρ to direct $\pi\pi$ amplitudes, $|B/A| = 0.79 \pm 0.01$ $(stat.) \pm 0.08$ $(syst.)$ $(\mathrm{GeV/c^2})^{-1/2}$ agrees, within errors, with the value reported in the previous STAR publication [8]: $(0.89 \pm 0.08$ $(stat.) \pm 0.09$ $(syst.)(\mathrm{GeV/c^2})^{-1/2})$. The same ratio, measured at 2.76 TeV/nucleon by ALICE, was found to be smaller $|B/A| = 0.50 \pm 0.04$ $(stat.)^{+0.10}_{-0.04}$ $(syst.)(\mathrm{GeV/c^2})^{-1/2})$ [9].

The ratio of ω to ρ amplitude was measured to be $C/A = 0.36 \pm 0.03$ $(stat.) \pm 0.04$ $(syst.)$. The ω amplitude is small, but is clearly visible through its interference with the ρ. This interference produces a small kink in the spectrum just above 800 MeV/c^2. The ω amplitude agrees with a prediction from STARlight [5], $C/A = 0.32$, which uses the $\gamma p \to \omega p$ cross section, and a classical Glauber calculation.

The only previous measurement of ρ-ω interference in the $\pi^+\pi^-$ channel was made by a DESY-MIT group, using 5-7 GeV photon beams [28]. That fit used a similar but not identical fit function, and found, neglecting differences in the treatment of the ω width, that $|C/A| = 0.36 \pm 0.04$. In the terminology of Ref. [28] $|C/A| = \zeta\sqrt{M_\rho\Gamma_\rho/M_\omega\Gamma_\omega}/\sqrt{(Br(\omega \to \pi\pi)}$.

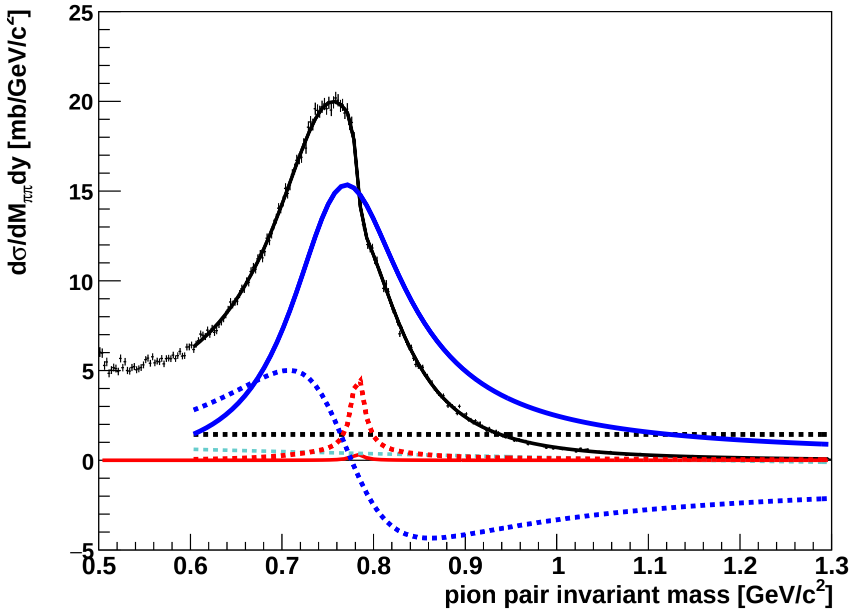

Figure 4: The $\pi^+\pi^-$ invariant-mass distribution for all selected $\pi\pi$ candidates with $p_T < 100$ MeV/c. The black markers show the data (in 2.5 MeV/c^2 bins). The black curve is the modified Söding fit to the data in the range $0.6 < M_{\pi\pi} < 1.3$ GeV. The ρ^0 Breit-Wigner component of the fitted function is shown with a blue curve and the constant non-resonant pion pair component is displayed with a black-dashed one. The interference between non-resonant pion pairs and the ρ^0 meson is shown with a blue-dashed curve. The Breit-Wigner distribution for the ω mesons is shown with a red curve and the interference between ρ^0 and ω is shown with a red-dashed curve. A small first order polynomial shown with a cyan-dashed curve accounts for the remnant background.

The fit finds a non-zero ω phase angle, $\phi_\omega = 1.46 \pm 0.11(stat.) \pm 0.07(syst.)$. The systematic error was estiamated from fits using slightly different fit functions. This phase angle result is a bit lower than the DESY-MIT measurement of of 1.68 ± 0.26. This agreement is still better than might be expected, since the DESY-MIT experiment used much lower energy photons, in a regime where production proceeds via both single meson and Pomeron exchange. Other experiments have studied ρ-ω interference using photoproduction to the e^+e^- final state (where the ω is more visible but the branching ratios are much smaller), or via the reaction $e^+e^- \to \pi^+\pi^-$, and found similar phase angles [32].

An alternate fit was performed, where $B_{\pi\pi}$ was multiplied by a mass dependent term, $(M_\rho/M_{\pi\pi})^2[(M_{\pi\pi}^2/4 - m_\pi^2)/(M_\rho^2/4 - m_\pi^2)]^{3/4}$ [33] to account for the possibility that the continuum $\pi\pi$ pairs do not completely interfere with the ρ or ω. This fit produced similar results, with a comparable‘ χ^2/DOF.

To study the photon energy dependence of the amplitude ratios, we performed the fit in five bins of rapidity: $|y| < 0.15$, $0.15 < |y| < 0.35$, and

Fit Parameter	value	units
M_ρ	0.7762 ± 0.0006	GeV/c^2
Γ_ρ	0.156 ± 0.001	GeV/c^2
A_ρ	1.538 ± 0.005	
$B_{\pi\pi}$	-1.21 ± 0.01	(GeV/c^2)$^{-1/2}$
C_ω	0.55 ± 0.04	
M_ω	0.7824 ± 0.0008	GeV/c^2
Γ_ω	0.017 ± 0.002	GeV/c^2
ϕ_ω	1.46 ± 0.11	radians
$f_p\ p_0$	0.99 ± 0.07	$(\mathrm{GeV}/c^2)^{-1}$
$f_p\ p_1$	-0.86 ± 0.06	$(\mathrm{GeV}/c^2)^{-2}$

Table 2: Results of fitting Eq. 2 to the data. The parameters p_0, p_1 and p_2 are for the the polynomial background.

Rapidity	Photon Energy (lab frame) MeV	γN center of mass energy GeV
0	380	12.4
0.15	327	11.5
	441	13.4
0.4	255	10.2
	488	14.1
0.63	202	9.1
	713	17.0

Table 3: Photon energy (lab frame), and γN center of mass energy for different rapidities . There are two rows per rapidity, one for the higher energy photon solution, and one for the lower

$|y| > 0.35$. These bins were chosen so that each bin had close to 100,000 pion pairs. To ensure the fits were stable, the values of M_ω and Γ_ω were fixed to the values extracted from the fit to the rapidity integrated pion pair mass distribution. The amplitudes should be symmetric around $y = 0$; pairing by $|y|$ provides a check on rapidity-dependent systematic errors.

In the lab frame, at low p_T, the rapidity is related to photon energy k by

$$k = M_{\pi\pi}/2 \exp{(\pm y)}. \tag{6}$$

The $\pm$ sign reflects the two-fold ambiguity as to which nucleus emitted the photon. Table 3 shows the conversion between rapidity, lab-frame photon energy, and photon-nucleon center of mass energy. Away from $y = 0$, the cross section is dominated by the lower photon energy; the relative fractions scale roughly as the ratio of the lab-frame photon energies. Table 3 gives the lab-frame photon energies and the γN center of mass energies for the two solutions to Eq. 6 for centers of the rapidity bins.

Figure 5 shows the ratios $|B/A|$ and C/A in the five rapidity bins. Both $|B/A|$ and C/A are flat as rapidity varies within the total errors, showing that

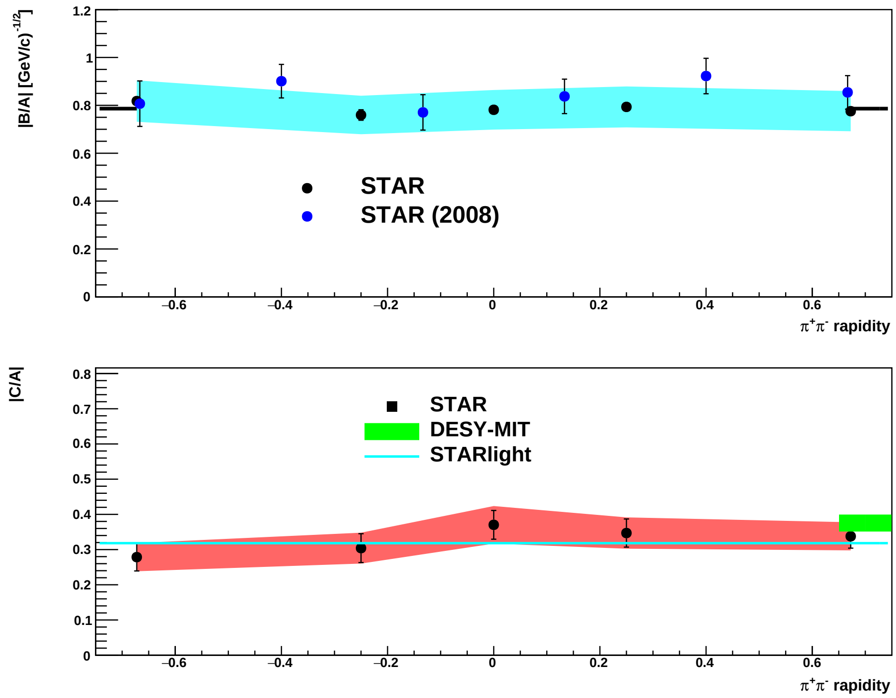

Figure 5: (Top) The ratio $|B/A|$ of amplitudes of non-resonant $\pi^+\pi^-$and ρ^0 mesons. The black points (with shaded blue systematic error band) are from the current analysis, while the previous STAR results are shown with blue-filled circles. The thick black line shows the rapidity-averaged result. In the bottom panel, the black points show the ratio $|C/A|$ of the ω to ρ^0 amplitude. The red band shows the systematic errors, while the horizontal blue line shows the STARlight prediction with the most recent branching ratio for $\omega \to \pi^+\pi^-$ decay [31]. The green band shows the DESY-MIT result for $|C/A|$ [28]. This result was at much lower photon energies leads to a large effective rapidity. For the lower energy photon solution of the two-fold ambiguity, the effective rapidity would be about -2.5.

these ratios do not have a large dependence on the photon energy. Also shown, are the STARlight predictions, and, for C/A, the DESY-MIT result. The DESY-MIT result is at a much lower beam energy which would correspond to an effective rapidity of -2.5 per the lower photon energy solution of Eq. 6.

To determine the ρ^0 cross section as a function of rapidity, we integrate the ρ Breit-Wigner function over the mass range from $2M_\pi$ to $M_\rho + 5\Gamma_\rho$. Because of the interference, we cannot separate the ρ^0, direct $\pi\pi$ and ω components in any given mass range. Instead, for the remaining results presented here, we determine the ratio of the ρ^0 cross section to the total $\pi^+\pi^-$ cross section - about 0.75 - and apply that ratio to determine the results that follow.

Figure 6 shows the acceptance corrected distribution of ρ^0 mesons detected in events with only two tracks from the triggered vertex. The asymmetry between positive and negative rapidity gives a measure of the rapidity-dependent systematic uncertainties in the cross section. These are likely due to asymmetries in the as-built longitudinal position of the TOF counters. The magnitude of this uncertainty grows slowly from mid-rapidity to reach a value of 4% at $y = 0.7$. Since the actual lengths of the TOF slats are known, this uncertainty does not apply for rapidity-integrated measurements.

The systematic uncertainties in these measurements fall into two classes, either an overall scale for the cross section, or uncertainties that vary point-to-point. The former is usually dominant.

The uncertainty in the integrated luminosity is 10%. As with previous measurements [8], this uncertainty is mainly driven by the fraction of the total Au+Au cross section accessible with the trigger used to collect this data. The selection of the number of neutrons produced in mutual electromagnetic dissociation is based on the ZDC calorimeters response. We allocate a 5% uncertainty to this neutron counting due to small non-linearities in the calorimeters and overlaps between one and many neutron distributions. We assign a 7% uncertainty due to modelling of the TOF system in the simulation, based on studies of the TOF response in more central collisions. The track reconstruction efficiency for the STAR TPC has a 3% per track uncertainty, for a total of 6% [19] while the efficiency of the vertex finder is known with a 5% uncertainty, driven by the effect of backgrounds. The uncertainty in how often the BBC detectors will veto good UPC events is due to fluctuating backgrounds. Even with use of embedding techniques, we estimate that these veto conditions introduce a 2% uncertainty to the results.

The same-sign pion pair distributions are the best estimators for the hadronic backgrounds for these two track events. The background subtraction was done at the level of raw histograms and also after a fit to the background to eliminate statistical fluctuations. These two procedures lead to final results that agree within 1.5%.

The scaling from the rapidity distribution extracted from 1n1n events to the previously measured XnXn distribution uses a correction, extracted from the event generator STARLight and introduces a 6% uncertainty related to the uncertainty in the neutron data used as input to STARlight. This uncertainty must be squared because we detect neutrons in both beams. It applies only to the XnXn results.

Summing these systematic uncertainties in quadrature leads to a 18.2% overall common uncertainty. This uncertainty is a bit higher than in our comparable previous publication [8], largely because of additional uncertainties associated with the pileup and the more complex trigger which is required to deal with the higher luminosities. Table 4 summarizes all the common systematic uncertainties identified in this measurement.

The main point-to-point systematic uncertainties in the rapidity and p_T distributions come from the track selection and particle identification. The systematic uncertainties were evaluated by varying the track quality cuts and PID cuts around their central value in both the data and simulation, and seeing how the final results varies. Table 5 lists the point-to-point uncertainties in the rapidity distribution while Table 6 lists the point-to-point uncertainties for the

Name	Value	Comment
Luminosity	10.0%	
ZDC	5.0%	ADC ch. to num. neutrons
TOF geometry modeling	7.0%	
TPC tracking efficiency	6.0%	3.0% per track [19]
Vertex Finder efficiency	5.0%	Background driven
BBC veto in trigger	2.0%	Background driven
Efficiency determination	7.0%	Ev. Gen., Material budget
Conversion from $\pi\pi$ pairs to ρ yield	2.2%	Varying mass fit range
Background subtraction	1.5%	
STARLight model	6.0%	only for XnXn results
Quadrature Sum	18.2%	

Table 4: Summary of all common systematic uncertainties identified in the generation of the rapidity distribution shown in Fig. 6 and the $-t$ distributions shown in Figs. 7 and 8. All these uncertainties are presented as percent fractions of the measured quantities.

Rapidity	PID cut	Fit to eff.	Number of track hits	TOF asymmetry
-0.70, -0.5	8.%	0.25%	0.2%	5%
-0.5, 0.	5.%	0.25%	0.05%	3.6%
0., 0.5	5.%	0.25%	0.05%	3.6%
0.5 - 0.7	8.%	0.25%	0.2%	5%

Table 5: Point-to-point systematic uncertainties on $d\sigma/dy$ (Fig. 6), as a percent of the measured cross section in four rapidity ranges. PID cut refers to uncertainty in the efficiency for π identification via the truncated dE/dx [34]. Those cuts were varied simultaneously in the data and simulation to determine the uncertainty due to particle identification. The fit to efficiency is the uncertainty in the parameterization of the efficiency, while the number of track hits refers to the minimum number of points used for fitting the track. The TOF asymmetry is the uncerainty due to the positions of the TOF slats. The actual $d\sigma/dy$ is symmetric around $y = 0$; the observed asymmetry is used as a measure of the systematic uncertainty from the TOF system.

p_T distribution.

The ALICE collaboration has also studied ρ photoproduction, in lead-lead collisions at the Large Hadron Collider (LHC) [9]. They fit their dipion mass distribution in the range from 0.6 to 1.5 GeV^2 to a function like Eq. 2, but without the ω component, finding masses and widths consistent with the standard values. Their cross-section values, $d\sigma/dy$ were about 10% above the STARlight prediction.

4. $d\sigma/dt$

Figure 7 shows the differential cross section $d\sigma/dt$ for ρ^0 mesons without any rapidity cut within the measured range $|y| < 1$, after like-sign background subtraction. The Mandelstam variable $t = t_\parallel + t_\perp$ with $t_\parallel = -M_\rho^2/(\gamma^2 e^{\pm y})$ and $t_\perp = -(p_T^{pair})^2$. At RHIC energies, $t_\parallel$ is almost negligible. $d\sigma/dt$ for ρ^0 mesons is obtained from a simple scaling by a common factor of 0.75. This

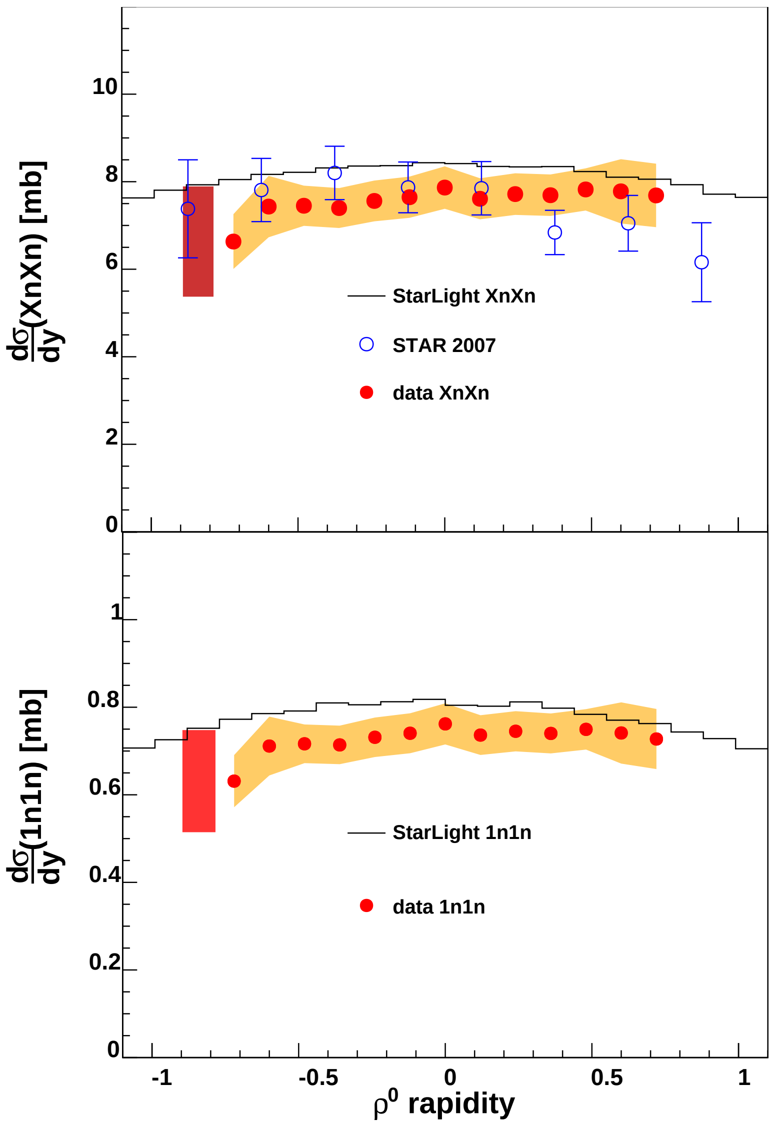

Figure 6: $d\sigma/dy$ for exclusively photoproduced ρ^0 mesons in (top) XnXn events and (bottom) 1n1n events. The data are shown with red markers. The statistical errors are smaller than the symbols, the orange band shows the quadrature sum of the point-to-point systematic uncertainties. The red box at $y \sim -0.9$ shows the quadrature sum of the common systematic uncertainties. The black histograms are the STARlight calculation for ρ^0 mesons with mutual dissociation. The blue markers in the top panel show the previous STAR measurement [8].

factor was extracted from comparisons between the number of pion pairs with invariant masses ranging from 500 MeV/c^2 to 1.5 GeV/c^2 and the integral of the ρ^0 Breit-Wigner function extracted from fits in rapidity and -t bins. In all comparisons, the integrals are performed from $2M_\pi$ to $M_\rho + 5\Gamma_\rho$. $d\sigma/dt$ is also corrected for the compounded effects of tracking reconstruction and geometrical acceptance, vertex finding efficiency and the finite track and TOF detector matching efficiency extracted from the embedded simulations. This correction is flat in t and has an average value of 6.4% over all rapidity values. Finally the distribution is normalized by the luminosity integrated over all data runs used in this analysis. The large peak in $d\sigma/dt$ for $|t| < 0.02\mathrm{GeV}^2$ is expected from coherent photoproduction. At substantially larger $|t|$, production should be dominated by incoherent interactions with individual nucleons in the target ion. At still higher $|t|$ (not seen here), individual partons should play a role.

We separate the ρ^0 t spectrum into coherent and incoherent components based on the shape of the distribution in Fig. 7. Because of the neutron requirement in the trigger, and the presence of Coulomb excitation, we cannot use the presence of neutrons from nuclear breakup as an event-by-event sign of incoherence [35].

The incoherent components for the 1n1n and XnXn distributions are fit with the so called "dipole" form factor

$$\frac{d\sigma}{dt} = \frac{A/Q_0^2}{(1+|t|/Q_0^2)^2} \tag{7}$$

used to describe low Q^2 photon-nucleon interactions [36]. The fit range for the incoherent events starts at $-t = 0.2$ GeV^2 (above the coherent production region) and extends to $-t = 0.45$ GeV^2 as shown by the black curve in the figure. The upper limit in t is chosen to reduce the contamination from hadronic interactions. For the events with mutual dissociation into any number of neutrons (XnXn), the fit finds $A = 3.46 \pm 0.02$ mb and $Q_0^2 = 0.099 \pm 0.015$ (GeV/c)^2 , with $\chi^2/NDF = 19/9$. For events with mutual dissociation into single neutrons (1n1n), the fit parameters are: $A = 0.191 \pm 0.003$ mb and $Q_0^2 = 0.099$ (fixed) (GeV/c)^2, with $\chi^2/NDF = 15.8/10$. The integral of the fit to the incoherent component in the XnXn events results in a value of cross section $\sigma_{incoh} = 2.89 \pm 0.02$ $(stat.) \pm 0.54$ $(syst.)$ mb. The integral of the coherent component discussed below amounts to 6.49 ± 0.01 $(stat.) \pm 1.18$ $(syst.)$ mb. The integral of the fit to the incoherent component in the 1n1n events results in a value of cross section $\sigma_{incoh} = 0.162 \pm 0.010$ $(stat.) \pm 0.029$ $(syst.)$ mb. The integral of the 1n1n coherent component amounts to 0.770 ± 0.004 $(stat.) \pm 0.140$ $(syst.)$ mb.

The corresponding ratios are:

$$\sigma^{XnXn}_{incoherent}/\sigma^{XnXn}_{coherent} = 0.445 \pm 0.015(stat.) \pm 0.005(syst.)$$

$$\sigma^{1n1n}_{incoherent}/\sigma^{1n1n}_{coherent} = 0.233 \pm 0.007(stat.) \pm 0.007(syst.).$$

Here, most of the systematic uncertainties cancel in the ratios.

The difference between the ratios for 1n1n and XnXn collisions is somewhat larger than were found in a previous STAR analysis [8]. This difference could come from a variety of sources. First, at large $|t|$, it is possible for a single photon to both produce a ρ^0 and leave the target nucleus excited, breaking the assumed factorization paradigm. The rate has not been calculated for ρ^0, but the cross section for J/ψ photoproduction accompanied by neutron emission is significant [37]. This calculated J/ψ cross section is noticeably less than for > 1 neutron emission, so ρ^0 photoproduction accompanied by neutron emission might alter the XnXn cross section ratio more than the 1n1n.

Second, unitarity corrections could play a role by changing the impact parameter distributions for 1n1n and XnXn interactions. Near grazing incidence, the cost of introducing another low-energy photon into the reaction is small. So, one photon can excite a nucleus, for example to a GDR, while a second photon can excite the nucleus further, leading to Xn emission rather than 1n [18]. The additional photon alters the impact parameter distributions for the 1n1n and XnXn channels; the XnXn channel will experience a slightly larger reduction at small $|t|$ due to interference from the two production sites; this may lead to slightly different measured slopes and coherent/incoherent ratios.

The coherent component of the t distribution is then extracted by subtracting the incoherent-component "dipole" form factor fit from the total $d\sigma/dt$. The resulting differential cross section for ρ^0 photoproduction acompanied with mutual dissociation of the nuclei into any number of neutrons (XnXn) and only one neutron (1n1n) is shown in Fig. 8 with red and black markers respectively. In both 1n1n and XnXn events, two well defined minima can clearly be seen. In both spectra, the first minima is at $-t = 0.018 \pm 0.005$ (GeV/c)$^{-2}$. A second minima is visible at 0.043 ± 0.01 (GeV/c)$^{-2}$. To first order, the gold nuclei are beginning to show signs of acting like black disks, with similar behavior for 1n1n and XnXn interactions.

A similar first minimum may be visible in ALICE data. Figure 3 of Ref. [9] shows an apparent dip in dN/dp_T for ρ photoproduction, around $p_T = 0.12$ GeV/c ($-t = 0.014$ GeV^2). This is for lead-lead collisions; lead nuclei are slightly larger than gold nuclei, so the dip should be at smaller t.

These minima are shallower than would be expected for $\gamma - A$ scattering, because the photon p_T partly fills in the dips in the $\gamma - A$ p_T spectrum. There are several theoretical predictions about the location and depth of these dips. One of them found the correct depths, but slightly different locations [38]. A quantum Glauber calculation which assumed nuclear shadowing did a better job of predicting the locations of the first minimum [11], although that calculation did not include the photon p_T, so missed the depth of the minimum. The Sar*t*re event generator run in UPC mode at RHIC energies [39] produces a Au nucleus recoil after ρ^0 elastic scattering with a very good agreement with the ρ^0 t distribution presented here.

An exponential function is used to characterize the spectrum below the first peak ($0.0024 < |t| < 0.0098$ (GeV/c)^2). There, the measured slope is 426.4 ± 1.8 (GeV/c)$^{-2}$ for the XnXn events and 407.8 ± 3.2 (GeV/c)$^{-2}$ for the 1n1n events. The XnXn slope is very similar to the ALICE measurement of $426 \pm 6 \pm 15$

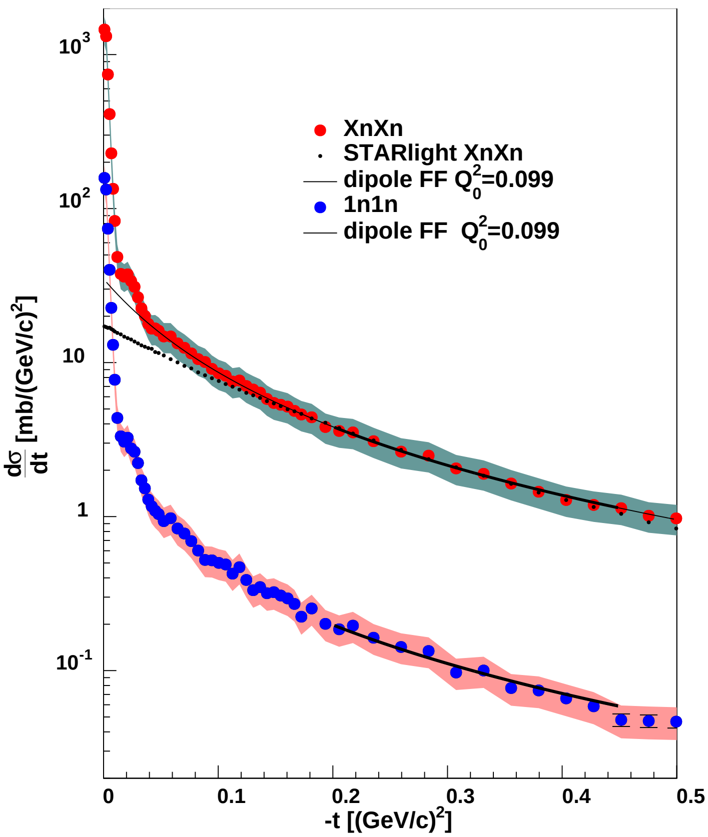

Figure 7: The -t distribution for exclusive ρ^0 mesons in events with 1n1n mutual dissociation (blue markers) or XnXn (red markers). Statistical errors are displayed with vertical line, and the colored bands show the total systematic uncertainties. The high t part of those distributions, which is dominated by the contribution from incoherent interactions, is fit to a dipole form factor, shown with a thin line. The STARlight prediction for the incoherent contribution is shown by the histogram with small black markers.

$-t[(\mathrm{GeV}/c)^2]$	track sel.	pion PID	Incoh. comp. sub.
0 - 0.02	0.2%	8%	0.5%
0.02 - 0.04	0.2%	8%	3.0%
0.04 - 0.1	0.2%	8%	8.5%

Table 6: Point-to-point systematic uncertainties for the $-t$ distribution shown in Fig. 8, as a percent of the measured cross section in three $-t$ ranges. The PID and track selection uncertainties are described in the text. The uncertainty in the incoherent component subtraction was estimated by selecting the biggest relative deviation from the default value and cross sections extracted by changing the value of the fit parameters by one standard deviation while the other parameters remain at the default fit value.

$(\mathrm{GeV/c})^{-2}$ [9]; there is no evidence for an increase in effective nuclear size with increasing photon energy.

At very small t, $|t| < 10^{-3}$ GeV^2, both cross sections flatten out and turn downward, as can be seen in the insert in Fig. 8. This is expected due to destructive interference between ρ production on the two nuclear targets [38, 40].

The systematic uncertainties in the differential cross sections come in two types, common uncertainties, from Tab. 4, and point-to-point uncertainties described above and listed in Table 6. The green and red bands in Fig. 8 are the sum in quadrature of all systematic uncertainties and statistical errors.

The shape of $d\sigma/dt$ for coherent photoproduction is determined by the position of the interaction sites within the target, and one can, in principle, determine the density distribution of the gold nucleus via a two dimensional Fourier transform of $d\sigma/dt$. The beam energies at RHIC are high enough so that, for ρ photoproduction at mid-rapidity, the longitudinal density distribution may be neglected and the ions may be treated as discs. Nuclei are azimuthally symmetric, so the radial distribution may be determined with a one-dimensional Fourier-Bessel (Hankel) transformation:

$$F(b) \propto \frac{1}{2\pi} \int_0^\infty dp_T p_T J_0(bp_T) \sqrt{\frac{d\sigma}{dt}} \tag{8}$$

Figure 9 shows the result of a numerical calculation of this transform in the region $|t| < 0.06$ GeV^2. The tails of $F(b)$ are negative around $|b|$=10 fm. This may be due to interference between the two nuclei. The decrease in $d\sigma/dt$ at very small t is due to what is effectively a negative amplitude coming in from the 'other' nucleus [40].

We varied the maximum t used for the transform over the range 0.05 to 0.09 GeV^2; this led to substantial variation at small b, shown by the cyan region in Fig. 9. The origin of this variation is not completely clear, but it may be related to aliasing due to the lack of a windowing function [41], or because of the limited statistics at large t. There is much less variation at the edges of the distribution. This leads us to believe that the transform can be used in the region where b ranges from $\sim 4 - 7$ fm. In this region, the full-width half-maximum (FWHM) of the distribution is $2 \times (6.17 \pm 0.12)$ fm. This FWHM is a measure of the hadronic size of the gold nucleus. With theoretical input, it could

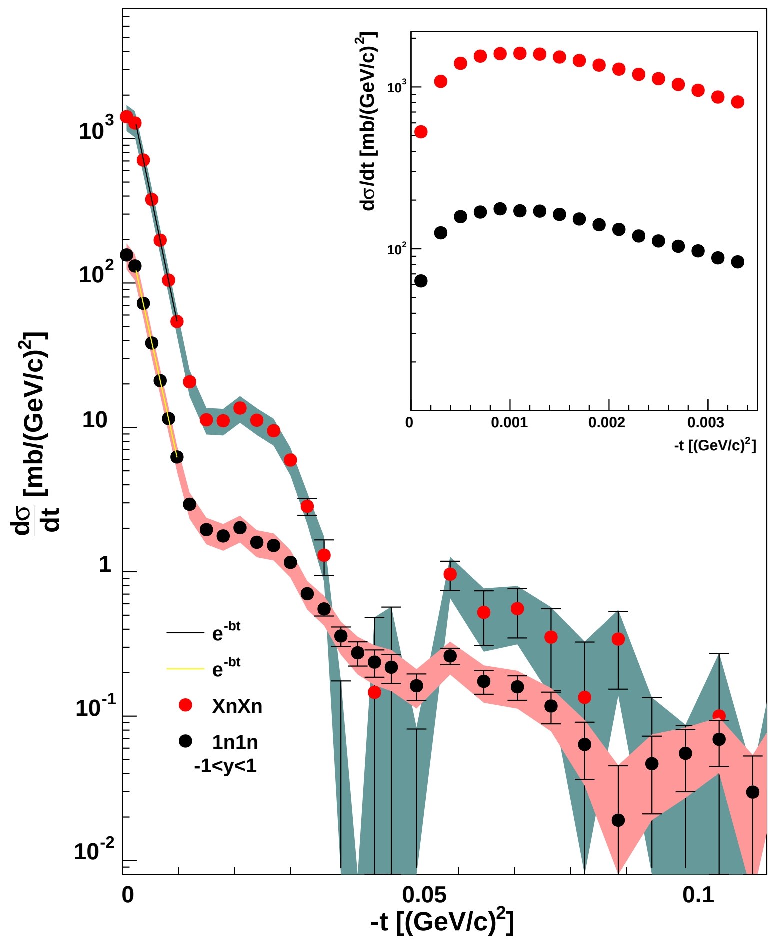

Figure 8: Fully normalized coherent diffraction patterns for ρ^0 mesons detected in exclusive XnXn events is shown with red markers. The same distribution but extracted from 1n1n events is shown with black markers. The filled bands shows the sum in quadrature of all systematic uncertainties listed in table 5 and the statistical errors, which are shown as vertical lines.The insert shows, with finer binning at low p_T, the effects of the destructive interference between photoproduction with the photon emitted by any of the two ions.

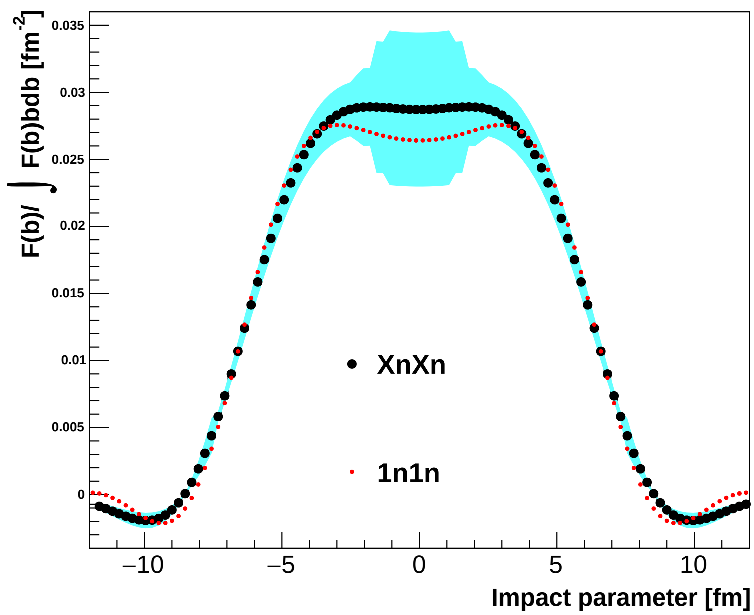

Figure 9: The normalized nucleon distribution in the transverse plane, the result of a two-dimensional Fourier transform (Hankel transform) of the XnXn and 1n1n diffraction patterns shown in Fig. 8. The integration is limited to a region where data is available, $0 < |t| < 0.06$ GeV^2. The cyan error band shows the effect of changing the maximum t to 0.05, 0.07 and 0.09 GeV^2. In order to highlight the similarity of both results at their falling edges, the resulting histograms are scaled by their integrals from -12 to 12 fm. The FWHM of both transforms is $2 \times (6.17 \pm 0.12)$ fm, consistent with the coherent diffraction of ρ^0 mesons off an object as big as the Au nuclei.

be compared with the electromagnetic (proton) radius of gold, as determined by electromagnetic scattering. The difference would be a measure of the neutron skin thickness of gold, something that is the subject of considerable experimental interest [42, 43].

Because of the possibility of ρ absorption the p_T introduced by the photon, the non-uniformity of the photon field (it is stronger on the 'near' side of the nucleus) and the effect of interference between the two production sites, care must be used in interpreting the transform.

5. Summary and Conclusions

In conclusion, STAR has made a precision study of ρ, ω and direct $\pi^+\pi^-$ photoproduction in 200 GeV/nucleon gold-on-gold ultra-peripheral collisions, using 394,000 $\pi^+\pi^-$ pairs.

We fit the invariant mass spectrum to a mixture of ρ, ω direct $\pi^+\pi^-$ and interference terms. The ratio of ρ to direct $\pi\pi$ is similar to that in previous measurements, while the newly measured ω contribution is comparable with predictions based on the previously measured $\gamma p \to \omega p$ cross section and the $\omega \to \pi^+\pi^-$ branching ratio. The relative fractions of ρ, ω and direct $\pi^+\pi^-$ do not vary significantly with rapidity, indicating that they all have a similar dependence on photon energy.

We also measure the cross section $d\sigma/dt$ over a wide range, and separate out coherent and incoherent components. The coherent contribution exhibits multiple diffractive minima, indicating that the nucleus is beginning to act like a black disk.

This measurement provides a nice lead-in to future studies of photo- and electro- production at an electron-ion collider (EIC) [44], where nuclei may be probed with photons at a wide range of Q^2 [45].

6. Acknowledgments

We thank the RHIC Operations Group and RCF at BNL, the NERSC Center at LBNL, the KISTI Center in Korea, and the Open Science Grid consortium for providing resources and support. This work was supported in part by the Office of Nuclear Physics within the U.S. DOE Office of Science, the U.S. NSF, the Ministry of Education and Science of the Russian Federation, NSFC, CAS, MoST and MoE of China, the National Research Foundation of Korea, NCKU (Taiwan), GA and MSMT of the Czech Republic, FIAS of Germany, DAE, DST, and UGC of India, the National Science Centre of Poland, National Research Foundation, the Ministry of Science, Education and Sports of the Republic of Croatia, and RosAtom of Russia.

References

[1] G. Baur, K. Hencken, D. Trautmann, S. Sadovsky, Y. Kharlov, Coherent gamma gamma and gamma-A interactions in very peripheral collisions at relativistic ion colliders, Phys.Rept. 364 (2002) 359–450. arXiv:hep-ph/0112211, doi:10.1016/S0370-1573(01)00101-6.

[2] C. A. Bertulani, S. R. Klein, J. Nystrand, Physics of ultra-peripheral nuclear collisions, Ann. Rev. Nucl. Part. Sci. 55 (2005) 271–310. arXiv:nucl-ex/0502005, doi:10.1146/annurev.nucl.55.090704.151526.

[3] J. Crittenden, Exclusive production of neutral vector mesons at the electron - proton collider HERAarXiv:hep-ex/9704009.

[4] J. Bartels, K. J. Golec-Biernat, H. Kowalski, A modification of the saturation model: DGLAP evolution, Phys.Rev. D66 (2002) 014001. arXiv:hep-ph/0203258, doi:10.1103/PhysRevD.66.014001.

[5] S. R. Klein, J. Nystrand, Exclusive vector meson production in relativistic heavy ion collisions, Phys. Rev. C 60 (1999) 014903. doi:10.1103/PhysRevC.60.014903.
URL http://link.aps.org/doi/10.1103/PhysRevC.60.014903

[6] G. Agakishiev, et al., ρ^0 Photoproduction in AuAu Collisions at $\sqrt{s_{NN}}$=62.4 GeV with STAR, Phys. Rev. C85 (2012) 014910. arXiv:1107.4630, doi:10.1103/PhysRevC.85.014910.

[7] C. Adler, et al., Coherent ρ^0 production in ultraperipheral heavy ion collisions, Phys. Rev. Lett. 89 (2002) 272302. arXiv:nucl-ex/0206004, doi:10.1103/PhysRevLett.89.272302.

[8] B. I. Abelev, et al., ρ^0 Photoproduction in Ultra-Peripheral Relativistic Heavy Ion Collisions with STAR, Phys. Rev. C77 (2008) 034910. arXiv:0712.3320, doi:10.1103/PhysRevC.77.034910.

[9] J. Adam, et al., Coherent ρ^0 photoproduction in ultra-peripheral Pb–Pb collisions at $\sqrt{s_{\rm NN}} = 2.76$ TeVarXiv:1503.09177.

[10] L. Frankfurt, M. Strikman, M. Zhalov, Predictions of the generalized Glauber model for the coherent rho production at RHIC and the STAR data, Phys. Rev. C67 (2003) 034901. arXiv:hep-ph/0210303, doi:10.1103/PhysRevC.67.034901.

[11] L. Frankfurt, V. Guzey, M. Strikman, M. Zhalov, Nuclear shadowing in photoproduction of ρ mesons in ultraperipheral nucleus collisions at RHIC and the LHCarXiv:1506.07150.

[12] V. P. Goncalves, M. V. T. Machado, Photoproduction of ρ^0 meson in ultra-peripheral heavy ion collisions at the BNL RHIC and CERN LHC, Phys. Rev. C80 (2009) 054901. arXiv:0907.4123, doi:10.1103/PhysRevC.80.054901.

[13] G. Sampaio dos Santos, M. V. T. Machado, Light vector meson photoproduction in hadron-hadron and nucleus-nucleus collisions at energies available at the CERN Large Hadron Collider, Phys. Rev. C91 (2) (2015) 025203. arXiv:1407.4148, doi:10.1103/PhysRevC.91.025203.

[14] M. Klusek-Gawenda, A. Szczurek, $\pi^+\pi^-$ and $\pi^0\pi^0$ pair production in photon-photon and in ultraperipheral ultrarelativistic heavy ion collisions, Phys. Rev. C87 (5) (2013) 054908. arXiv:1302.4204, doi:10.1103/PhysRevC.87.054908.

[15] B. L. Berman, S. C. Fultz, Measurements of the giant dipole resonance with monoenergetic photons, Rev. Mod. Phys. 47 (1975) 713–761. doi:10.1103/RevModPhys.47.713.
URL http://link.aps.org/doi/10.1103/RevModPhys.47.713

[16] G. Baur, K. Hencken, A. Aste, D. Trautmann, S. R. Klein, Multiphoton exchange processes in ultraperipheral relativistic heavy ion collisions, Nucl. Phys. A729 (2003) 787–808. arXiv:nucl-th/0307031, doi:10.1016/j.nuclphysa.2003.09.006.

[17] A. J. Baltz, S. R. Klein, J. Nystrand, Coherent vector meson photoproduction with nuclear breakup in relativistic heavy ion collisions, Phys. Rev. Lett. 89 (2002) 012301. arXiv:nucl-th/0205031, doi:10.1103/PhysRevLett.89.012301.

[18] A. J. Baltz, M. J. Rhoades-Brown, J. Weneser, Heavy ion partial beam lifetimes due to Coulomb induced processes, Phys. Rev. E54 (1996) 4233–4239. doi:10.1103/PhysRevE.54.4233.

[19] M. Anderson, et al., The Star time projection chamber: A Unique tool for studying high multiplicity events at RHIC, Nucl.Instrum.Meth. A499 (2003) 659–678. arXiv:nucl-ex/0301015, doi:10.1016/S0168-9002(02)01964-2.

[20] W. J. Llope, The large-area time-of-flight upgrade for STAR, Nucl. Instrum. Meth. B241 (2005) 306–310. doi:10.1016/j.nimb.2005.07.089.

[21] J. Kiryluk, Local polarimetry for proton beams with the STAR beam beam counters, in: Spin physics. Polarized electron sources and polarimeters. Proceedings, 16th International Symposium, SPIN 2004, Trieste, Italy, October 10-16, 2004, and Workshop, PESP 2004, Mainz, Germany, October 7-9, 2004, 2005, pp. 718–721. arXiv:hep-ex/0501072.

[22] C. Adler, A. Denisov, E. Garcia, M. Murray, H. Strobele, S. White, The RHIC zero-degree calorimeters, Nucl. Instrum. Meth. A499 (2003) 433–436. doi:10.1016/j.nima.2003.08.112.

[23] F. S. Bieser, et al., The STAR trigger, Nucl. Instrum. Meth. A499 (2003) 766–777. doi:10.1016/S0168-9002(02)01974-5.

[24] S. R. Klein, J. Nystrand, J. Seger, Y. Gorbunov, J. Butterworth, STARlight: A Monte Carlo simulation program for ultra-peripheral collisions of relativistic ionsarXiv:1607.03838.

[25] I. A. Pshenichnov, J. P. Bondorf, I. N. Mishustin, A. Ventura, S. Masetti, Mutual heavy ion dissociation in peripheral collisions at ultrarelativistic energies, Phys. Rev. C64 (2001) 024903. arXiv:nucl-th/0101035, doi:10.1103/PhysRevC.64.024903.

[26] M. Klusek-Gawenda, M. Ciemala, W. Schafer, A. Szczurek, Electromagnetic excitation of nuclei and neutron evaporation in ultrarelativistic ultraperipheral heavy ion collisions, Phys. Rev. C89 (5) (2014) 054907. arXiv:1311.1938, doi:10.1103/PhysRevC.89.054907.

[27] P. Soding, On the Apparent shift of the rho meson mass in photoproduction, Phys. Lett. 19 (1966) 702–704. doi:10.1016/0031-9163(66)90451-3.

[28] H. Alvensleben, et al., Precise determination of rho-omega interference parameters from photoproduction of vector mesons off nucleon and nuclei, Phys. Rev. Lett. 27 (1971) 888–892. doi:10.1103/PhysRevLett.27.888.

[29] E. A. Kuraev, Z. K. Silagadze, Once more about the omega —¿ 3 pi contact term, Phys. Atom. Nucl. 58 (1995) 1589–1596, [Yad. Fiz.58N9,1687(1995)]. arXiv:hep-ph/9502406.

[30] R. R. Akhmetshin, et al., Measurement of omega meson parameters in pi+ pi- pi0 decay mode with CMD-2, Phys. Lett. B476 (2000) 33–39. arXiv:hep-ex/0002017, doi:10.1016/S0370-2693(00)00123-4.

[31] K. A. Olive, et al., Review of Particle Physics, Chin. Phys. C38 (2014) 090001. doi:10.1088/1674-1137/38/9/090001.

[32] P. Langacker, Quark Mass Differences and $\rho - \omega$ Mixing, Phys. Rev. D20 (1979) 2983. doi:10.1103/PhysRevD.20.2983.

[33] J. Pumplin, Diffraction dissociation and the reaction $\gamma p \to \pi^+\pi^- p$, Phys. Rev. D2 (1970) 1859. doi:10.1103/PhysRevD.2.1859.

[34] Y. Xu, O. Barannikova, H. Bichsel, X. Dong, P. Fachini, Y. Fisyak, A. Kocoloski, B. Mohanty, P. Netrakanti, L. Ruan, M. C. Suarez, Z. Tang, G. van Buren, Z. Xu, Nuclear Instruments and Methods in Physics Research Section A: Accelerators, Spectrometers, Detectors and Associated Equipment 614 (1) (2010) 28 – 33. doi:http://dx.doi.org/10.1016/j.nima.2009.12.011, [link].
URL http://www.sciencedirect.com/science/article/pii/S0168900209023067

[35] V. Rebyakova, M. Strikman, M. Zhalov, Coherent ρ and J/ψ photoproduction in ultraperipheral processes with electromagnetic dissociation of heavy ions at RHIC and LHC, Phys. Lett. B710 (2012) 647–653. arXiv:1109.0737, doi:10.1016/j.physletb.2012.03.041.

[36] M. Drees, D. Zeppenfeld, Production of supersymmetric particles in elastic ep collisions, Phys. Rev. D 39 (1989) 2536–2546. doi:10.1103/PhysRevD.39.2536.
URL http://link.aps.org/doi/10.1103/PhysRevD.39.2536

[37] M. Strikman, M. Tverskoy, M. Zhalov, Neutron tagging of quasielastic J/psi photoproduction off nucleus in ultraperipheral heavy ion collisions at RHIC energies, Phys. Lett. B626 (2005) 72–79. arXiv:hep-ph/0505023, doi:10.1016/j.physletb.2005.08.083.

[38] S. R. Klein, J. Nystrand, Interference in exclusive vector meson production in heavy ion collisions, Phys. Rev. Lett. 84 (2000) 2330–2333. arXiv:hep-ph/9909237, doi:10.1103/PhysRevLett.84.2330.

[39] T. Toll, T. Ullrich, The dipole model Monte Carlo generator Sartre 1, Comput.Phys.Commun. 185 (2014) 1835–1853. arXiv:1307.8059, doi:10.1016/j.cpc.2014.03.010.

[40] B. I. Abelev, et al., Observation of Two-source Interference in the Photoproduction Reaction Au Au —¿ Au Au ρ^0, Phys. Rev. Lett. 102 (2009) 112301. arXiv:0812.1063, doi:10.1103/PhysRevLett.102.112301.

[41] Window Function.
URL https://en.wikipedia.org/wiki/Window_function

[42] C. M. Tarbert, et al., Neutron skin of ^{208}Pb from Coherent Pion Photoproduction, Phys. Rev. Lett. 112 (24) (2014) 242502. arXiv:1311.0168, doi:10.1103/PhysRevLett.112.242502.

[43] A. Gardestig, C. J. Horowitz, G. A. Miller, Comment on "Neutron Skin of ^{208}Pb from Coherent Pion Photoproduction"arXiv:1504.08347.

[44] A. Accardi, et al., Electron Ion Collider: The Next QCD Frontier - Understanding the glue that binds us allarXiv:1212.1701.

[45] T. Toll, T. Ullrich, Exclusive diffractive processes in electron-ion collisions, Phys.Rev. C87 (2) (2013) 024913. arXiv:1211.3048, doi:10.1103/PhysRevC.87.024913.